

# Ordered Mesoporous Silica to Study the Preparation of Ni/SiO<sub>2</sub> ex Nitrate Catalysts: Impregnation, Drying, and Thermal Treatments

Jelle R. A. Sietsma, Johannes D. Meeldijk, Marjan Versluijs-Helder, Alfred Broersma, A. Jos van Dillen, Petra E. de Jongh, and Krijn P. de Jong\*

*Inorganic Chemistry and Catalysis, Utrecht University, Sorbonnelaan 16, P.O. Box 80083, 3508 TB Utrecht, The Netherlands*

*Received September 12, 2007. Revised Manuscript Received January 16, 2008*

In this contribution, we investigated the preparation of Ni/SiO<sub>2</sub> catalysts with aqueous [Ni(OH)<sub>2</sub>]<sub>6</sub>(NO<sub>3</sub>)<sub>2</sub> solutions via the impregnation and drying method using ordered mesoporous silica SBA-15 (mesopore diameter of 9 nm) as model support to study each step in the preparation: impregnation, drying, calcination, and reduction. After impregnation, not all the mesopores of SBA-15 appeared filled with precursor solution. Consecutive drying led to formation of 9 nm Ni<sub>3</sub>(NO<sub>3</sub>)<sub>2</sub>(OH)<sub>4</sub> crystallites exclusively within the mesopores. During air calcination, severe sintering and redistribution took place, resulting in a low NiO dispersion, including large NiO crystals outside of the mesopores and rodlike NiO particles inside the mesopores. The degree of sintering depended on the concentration of Ni<sub>3</sub>(NO<sub>3</sub>)<sub>2</sub>(OH)<sub>4</sub> decomposition products (NO<sub>2</sub>, N<sub>2</sub>O, O<sub>2</sub> and H<sub>2</sub>O), and in particular NO<sub>2</sub> and O<sub>2</sub> were found to promote sintering and redistribution. Therefore, maintaining low concentrations of the latter components during the thermal nitrate decomposition is advocated, which was achieved by carrying out the treatment in the presence of H<sub>2</sub>. The latter treatment prevented formation of NO<sub>2</sub>/O<sub>2</sub> as decomposition products, moderated the decomposition rate of Ni<sub>3</sub>(NO<sub>3</sub>)<sub>2</sub>(OH)<sub>4</sub> into NiO as observed from in situ XRD experiments, and led to NiO particles of 3 nm on average at a loading of 20 wt % Ni/SiO<sub>2</sub>.

## Introduction

Supported metal (oxide) catalysts are essential for the production of fuels and chemicals, and the reduction of environmental pollution. Nickel-based catalysts are among the most widely used because of their activity in many important (de)hydrogenation reactions.<sup>1–3</sup> The metal is deposited onto a support like SiO<sub>2</sub> or Al<sub>2</sub>O<sub>3</sub> to achieve a high and thermally stable dispersion. Preparation techniques are primarily based on deposition of a precursor complex from the liquid phase and involve ion-adsorption,<sup>4,5</sup> deposition-precipitation,<sup>6–8</sup> and impregnation and drying.<sup>9–13</sup> Often, the latter is preferred because of its simplicity and the limited production of waste. After impregnation of a porous support

with a precursor-containing solution and subsequent drying, the product is typically heat treated in air, often referred to as calcination, to convert the precursor into the desired metal oxide, or metal when followed by a high-temperature reduction step with H<sub>2</sub>.

Landmark studies at low Ni loadings and strong precursor-support interactions have revealed much insight into the interplay between metal, ligands, counterions and supports, and their impact on the activity, selectivity, and stability of the final catalyst.<sup>8,11,12,14</sup> In addition, fundamental insight into the importance of liquid–solid interactions between support and the precursor solution on the formation of poorly reducible mixed Ni phases like aluminates or phyllosilicates has been obtained. However, at Ni loadings well above the ion-adsorption capacity of the support and with a weak precursor-support interaction, phenomena like redistribution and sintering during the successive (thermal) steps in the preparation might prevail. In this contribution we present a systematic study on the preparation of Ni/SiO<sub>2</sub> catalysts with loadings of 20–23 wt % prepared by the impregnation and drying method using aqueous [Ni(OH)<sub>2</sub>]<sub>6</sub>(NO<sub>3</sub>)<sub>2</sub> precursor solutions.

In principle, Ni(NO<sub>3</sub>)<sub>2</sub>·6H<sub>2</sub>O is an attractive precursor as its high solubility enables preparation of highly loaded Ni catalysts via a single-step impregnation. Moreover, it is cost-effective and pure NiO can be obtained because of the facile and complete removal of nitrate via thermal decomposition in air. Unfortunately, at loadings significantly higher than

\* Corresponding author. E-mail: k.p.dejong@uu.nl.

- (1) Balakos, M. W.; Hernandez, E. E. *Catal. Today* **1997**, *35*, 415–425.
- (2) Fouilloux, P. *Appl. Catal.* **1983**, *8*, 1–42.
- (3) Allen, R. R. *J. Am. Oil Chem. Soc.* **1986**, *63*, 1328–1332.
- (4) Schreier, M.; Regalbutto, J. R. *J. Catal.* **2004**, *225*, 190–202.
- (5) Carrier, X.; Lambert, J. F.; Che, M. *J. Am. Chem. Soc.* **1997**, *119*, 10137–10146.
- (6) Hermans, L. A. M.; Geus, J. W. *Stud. Surf. Sci. Catal.* **1979**, *3*, 113–130.
- (7) Van der Lee, M. K.; Van Dillen, A. J.; Bitter, J. H.; De Jong, K. P. *J. Am. Chem. Soc.* **2005**, *127*, 13573–13582.
- (8) Che, M.; Cheng, Z. X.; Louis, C. *J. Am. Chem. Soc.* **1995**, *117*, 2008–2018.
- (9) Bourikas, K.; Kordulis, C.; Lycourghiotis, A. *Catal. Rev.* **2006**, *48*, 363–444.
- (10) De Jong, K. P. *Curr. Opin. Solid State Mater. Sci.* **1999**, *4*, 55–62.
- (11) Clause, O.; Kermarec, M.; Bonnevoit, L.; Villain, F.; Che, M. *J. Am. Chem. Soc.* **1992**, *114*, 4709–4717.
- (12) Carriat, J. Y.; Che, M.; Kermarec, M.; Verdager, M.; Michalowicz, A. *J. Am. Chem. Soc.* **1998**, *120*, 2059–2070.
- (13) Lekhal, A.; Glasser, B. J.; Khinast, J. G. *Chem. Eng. Sci.* **2004**, *59*, 1063–1077.

- (14) Négrier, F.; Marceau, E.; Che, M.; Giraudon, J.-M.; Gengembre, G.; Löfberg, A. *J. Phys. Chem. B* **2005**, *109*, 2836–2845.

the support ion-adsorption capacity poorly dispersed Ni catalysts are generally obtained. Similar findings have been reported for a variety of metal nitrates, among which are those of cobalt,<sup>15,16</sup> iron,<sup>17</sup> and copper.<sup>18</sup> These results were obtained for both preshaped bodies (i.e., extrudates, pellets, and sol-gel spheres) and powder supports.

Although Ni(NO<sub>3</sub>)<sub>2</sub>·6H<sub>2</sub>O was already used in 1910 for the preparation of SiO<sub>2</sub> and Al<sub>2</sub>O<sub>3</sub> supported Ni catalysts,<sup>19</sup> thus far, little is known about the physicochemical process(es) responsible for its poor metal dispersion when treated through drying, calcination, and reduction. Moreover, little consensus is found among the reported studies. Some authors have stated that prevention of redistribution during drying is the key to obtain a highly dispersed and homogeneously distributed metal (oxide) phase. These findings are mainly based on comparison of extrudates, spheres, or pellets that were impregnated and dried using a metal nitrate (e.g., Ni or Fe) or citrate salt, and on the addition of polysaccharide carbohydrates (e.g., hydroxyethylcellulose) to Cu(NO<sub>3</sub>)<sub>2</sub>·6H<sub>2</sub>O precursor solutions.<sup>17,20–23</sup> These studies indicated that the use of chelating salts or the addition of viscosity-increasing agents to aqueous nitrate solutions prevented the formation of egg-shell type distributions. Besides homogeneous precursor distributions, the metal dispersion of the final catalyst was also found to increase largely with these chelating precursor salts. Lensveld and others showed that these findings could be transferred to powder supports based on silica gel.<sup>20,21</sup>

Other studies indicated that with metal nitrates a poor dispersion is obtained due to sintering during the calcination step.<sup>24–28</sup> Poels et al. concluded for Ni/Al<sub>2</sub>O<sub>3</sub> that a high concentration of NO<sub>x</sub> and/or H<sub>2</sub>O decomposition products during calcination had a detrimental effect on the ultimate dispersion.<sup>25,26</sup> Reinalda and Kars found similar results for Co/SiO<sub>2</sub> and used this property to obtain a more sintered Co metal phase.<sup>27</sup> In addition, Van de Loosdrecht et al. investigated the air space velocity and heating rate effects during calcination of supported Co(NO<sub>3</sub>)<sub>2</sub>·6H<sub>2</sub>O on the performance of the final Co catalysts in the Fischer–Tropsch synthesis, and observed that a low concentration of decom-

position products led to more active catalysts.<sup>28</sup> On the other hand Louis et al. suggested, for Ni/SiO<sub>2</sub>, that large particles are probably formed due to the partial decomposition during calcination of phyllosilicate anchoring sites for Ni.<sup>29</sup> Unfortunately, these studies have not disentangled the impact of the drying treatment on the dispersion on the one hand, and the influence of specific decomposition product(s) (e.g., O<sub>2</sub>, H<sub>2</sub>O, NO, NO<sub>2</sub> and N<sub>2</sub>O) on the sintering process during calcination, on the other hand.

The inconclusiveness regarding identification of the most detrimental process to the ultimate metal dispersion can be largely ascribed to limitations in techniques available to monitor the dispersion and distribution of precursor compounds on conventional supports. Many characterization techniques require special pretreatments; for instance insight into the dispersion by chemisorption can only be obtained after reduction of the precursor to the metal phase. Powder X-ray diffraction (XRD) renders an average crystallite size only if the precursor phase is crystalline. Electron microscopy could give direct accurate information on the precursor distribution over the support combined with particle size distributions. Unfortunately, the heterogeneity of conventional supports makes it cumbersome to obtain detailed information with this technique. A possibility to overcome this problem is at hand since the discovery in the early nineties of a new type of materials, namely, ordered mesoporous materials prepared via a templating mechanism.<sup>30</sup> Nowadays, a wide variety of ordered mesoporous materials is available. We propose that these supports provide model systems to study the individual steps in catalyst preparation. Especially for mesoporous silicas like MCM-41 and SBA-15, pore size and geometry are uniform, well-defined, and variable over a wide range.<sup>30,31</sup> These properties make it possible to obtain much more detailed information from TEM, as a clear differentiation can be made between precursor and support. Furthermore, the uniform pore system enables one to derive more detailed information from N<sub>2</sub>-physisorption experiments. Particle growth inside the mesoporous channels during preparation can be monitored as the degree of (partial) pore blocking by these guest phase particles and is displayed in the desorption branch of the isotherm.<sup>32–34</sup> An additional advantage of the uniform pore size involves the prevention of extensive migration of precursor during drying because differences in capillary suction between pores are lacking.<sup>35</sup> As a result, studies on the separate effect of impregnation, drying, and thermal treatments on the ultimate metal dispersion become within reach.

- (15) Wang, Y.; Noguchi, M.; Takahashi, Y.; Ohtsuka, Y. *Catal. Today* **2001**, *68*, 3–9.
- (16) Ohtsuka, Y.; Takahashi, Y.; Noguchi, M.; Arai, T.; Takasaki, S.; Tsubouchi, N.; Wang, Y. *Catal. Today* **2004**, *89*, 419–429.
- (17) Van den Brink, P. J.; Scholten, A.; Van Wageningen, A.; Lamers, M. D. A.; Van Dillen, A. J.; Geus, J. W. *Stud. Surf. Sci. Catal.* **1991**, *63*, 527–537.
- (18) Chen, H.-C.; Anderson, R. B. *J. Catal.* **1976**, *43*, 200–206.
- (19) Crosfield and Sons, Patent GB1030282, 1910.
- (20) Lensveld, D. J.; Mesu, J. G.; Van Dillen, A. J.; De Jong, K. P. *Microporous Mesoporous Mater.* **2001**, *44–45*, 401–407.
- (21) Infantes-Molina, A.; Mérida-Robles, J.; Braos-García, P.; Rodríguez-Castellón, E.; Finocchio, E.; Busca, G.; Maireles-Torres, P.; Jiménez-López, A. *J. Catal.* **2004**, *225*, 479–488.
- (22) Kotter, M.; Riekert, L. *Stud. Surf. Sci. Catal.* **1979**, *3*, 51–63.
- (23) Van Dillen, A. J.; Terörde, R.J.A.M.; Lensveld, D. J.; Geus, J. W.; de Jong, K. P. *J. Catal.* **2003**, *216*, 257–264.
- (24) Chen, I.; Lin, S.-Y.; Shiue, D.-W. *Ind. Eng. Chem. Res.* **1988**, *27*, 926–929.
- (25) Poels, E. K.; Dekker, J. G.; Van Leeuwen, W. A. *Stud. Surf. Sci. Catal.* **1991**, *63*, 205–214.
- (26) Vos, B.; Poels, E. K.; Bliet, A. *J. Catal.* **2001**, *198*, 77–88.
- (27) Reinalda, D.; Kars, J. Patent US 5,021,387, 1991.
- (28) Van de Loosdrecht, J.; Barradas, S.; Caricato, E. A.; Ngwenya, N. G.; Nkwanyana, P. S.; Rawat, M. A. S.; Sigwebela, B. H.; Van Berge, P. J.; Visagie, J. L. *Top. Catal.* **2003**, *26*, 121–127.

- (29) Louis, C.; Cheng, Z. X.; Che, M. *J. Phys. Chem.* **1993**, *97*, 5703–5712.
- (30) Kresge, C. T.; Leonowicz, M. E.; Roth, W. J.; Vartuli, J. C.; Beck, J. S. *Nature* **1992**, *359*, 710–712.
- (31) Zhao, D.; Feng, J.; Huo, Q.; Melosh, N.; Fredrickson, G. H.; Chmelka, B. F.; Stucky, G. D. *Science* **1998**, *279*, 548–552.
- (32) Ravikovitch, P. I.; Neimark, A. V. *Langmuir* **2002**, *18*, 9830–9837.
- (33) Van der Voort, P.; Ravikovitch, P. I.; De Jong, K. P.; Benjeloun, M.; Van Bavel, E.; Janssen, A. H.; Neimark, A. V.; Weckhuysen, B. M.; Vansant, E. F. *J. Phys. Chem. B* **2002**, *106*, 5873–5877.
- (34) Janssen, A. H.; Yang, C.-M.; Wang, Y.; Schuth, F.; Koster, A. J.; De Jong, K. P. *J. Phys. Chem. B* **2003**, *107*, 10552–10556.
- (35) Neimark, A. V.; Kheifetz, L. I.; Fenelonov, V. B. *Ind. Eng. Chem. Prod. Res. Dev.* **1981**, *20*, 439–450.

In this contribution, we demonstrate the potential of ordered mesoporous supports as model support systems for studying individual steps in catalyst preparation. As a case study we examined the preparation of Ni/SiO<sub>2</sub> catalysts by impregnation and drying using Ni(NO<sub>3</sub>)<sub>2</sub>·6H<sub>2</sub>O as precursor salt. We show that using silica-based SBA-15 we can identify the impact of individual treatments on the dispersion and distribution of the active phase or its precursor over the support. Moreover, results obtained with silica gel indicated that these findings are also relevant for conventional supports.

## Experimental Section

**Support Preparation.** SBA-15 (BET surface area = 637 m<sup>2</sup> g<sup>-1</sup>, pore volume = 0.80 mL g<sup>-1</sup>, and average pore diameter = 9 nm) was prepared following the procedure of Zhao et al.<sup>31</sup> PEO<sub>20</sub>PPO<sub>70</sub>PEO<sub>20</sub> (PEO = poly(ethylene oxide) and PPO = poly(propylene oxide)) triblock copolymer (Aldrich) was dissolved in 250 mL of demineralized water of 40 °C. After the solution had become clear, 48 g of concentrated HCl (Merck) was added, followed by the addition of 21.5 mL of tetraethyl orthosilicate (Acros). The mixture was stirred for 20 h at 40 °C and then transferred to an oven for further reaction at 80 °C for 48 h. The solid product was collected from the suspension by filtration, washed, dried in air for 12 h at 80 °C, and calcined for 6 h at 550 °C. Davicat 1404 silica gel (BET surface area = 500 m<sup>2</sup> g<sup>-1</sup>, pore volume = 0.90 mL g<sup>-1</sup> and average pore diameter = 7 nm) was used as received from Grace-Davison.

**Catalyst Preparation.** All samples were labeled using codes. An example of a code is S/D-C-R. The first part denotes the support: S = SBA-15 and G = silica gel support. The second part indicates the heat treatments that were applied: D = dried, C = thermally treated in air (i.e., calcined), and R = reduced with 5% v/v H<sub>2</sub>/Ar.

Prior to impregnation in a static vacuum, the supports were dried for 2 h at 80 °C in dynamic vacuum to remove physisorbed water. SBA-15 and silica gel were impregnated with 1 or 1.25 mL g<sup>-1</sup> of precursor solution, respectively. Aqueous [Ni(OH)<sub>2</sub>]<sub>6</sub>(NO<sub>3</sub>)<sub>2</sub> solution (4.2 M) was prepared by dissolving Ni(NO<sub>3</sub>)<sub>2</sub>·6H<sub>2</sub>O in demineralized water. After impregnation, the samples were dried in static air by heating with 1 °C min<sup>-1</sup> from room temperature to 120 °C and kept at that temperature for 12 h. Subsequent calcination treatments were carried out using a plug flow reactor (length 17 cm and diameter 1 cm) and varying airflows of 0–100 mL min<sup>-1</sup> by heating approximately 40 mg of the dried samples from room temperature to 450 °C with a ramp of 1 °C min<sup>-1</sup>. The samples were kept at 450 °C for 4 h. For thermal treatments in He, flows of 50 or 100 mL min<sup>-1</sup> were used, whereas for He diluted gas streams of NO<sub>2</sub>/O<sub>2</sub> (10/3% v/v) or H<sub>2</sub>O (15% v/v) a flow of 50 mL min<sup>-1</sup> was used. Calcination under stagnant conditions was carried out by heating 0.25 g of dried impregnate S/D in an oven dish (volume 0.062 dm<sup>3</sup>) with a loose lid on top to retard removal of the decomposition products. Reduction treatments were performed by heating of dried sample with 5 °C min<sup>-1</sup> to 600 °C, whereas a 5% H<sub>2</sub>/Ar flow of 50 mL min<sup>-1</sup> was passed through the sample bed. The reduced samples were passivated via controlled exposure to air. For calculation of the gas-hourly space-velocities (GHSV), apparent bulk densities of 0.46 and 0.09 g cm<sup>-3</sup> were used for silica gel and SBA-15, respectively.

Anhydrous Ni(NO<sub>3</sub>)<sub>2</sub> solution (1.35 M) was prepared by dissolving Ni(NO<sub>3</sub>)<sub>2</sub>·6H<sub>2</sub>O in dry ethanol. Subsequently, water present was removed by reaction with ethyl orthoformate<sup>36</sup> to form ethanol

and ethyl formate. The latter component was removed from the solution by vacuum distillation. Sample impregnated with the anhydrous Ni(NO<sub>3</sub>)<sub>2</sub> solution was dried using the same drying procedure only using a dry argon flow instead of static air. For calcination of the anhydrous Ni(NO<sub>3</sub>)<sub>2</sub> sample the air flow of 100 mL min<sup>-1</sup> was dried using a molsieve filter.

**Characterization.** N<sub>2</sub>-physisorption measurements were performed at -196 °C, using a Micromeritics Tristar 3000 apparatus. The samples were dried in He flow for 14 h at 120 °C prior to analysis. The pore size distribution was derived from the adsorption branch of the isotherm using a nonlocal density functional theory (NL-DFT) model for ordered mesoporous silicas with cylindrical pore geometry developed by Jaroniec et al.,<sup>37</sup> which showed to provide a reliable representation of the data. The pore diameter of the mesoporous channels of SBA-15 was defined by the value at which the maximum in differential pore volume was observed. The micro and meso-porosity were defined as the volume present in pores ≤ 2 nm, and between 2 and 50 nm, respectively. There is no standard method yet for the determination of blocked mesopore volume (V<sub>meso,bl</sub>), hence we used the BJH theory<sup>38</sup> with the Harkins and Jura<sup>39</sup> thickness equation and the Kruk-Jaroniec-Sayari correction<sup>40</sup> for ordered mesoporous siliceous materials to calculate from the desorption branch the cumulative pore volume as a function of the pore size. From this we determined the total amount of V<sub>meso,bl</sub> considering that the pores with a diameter of 2–5 nm are due to volume in (partially) blocked pores. Finally, mesopore and external surface areas were determined with the t-method using thickness ranges of 0.35–0.55 and 1.00–1.41 nm, respectively.<sup>41</sup>

Powder X-ray diffraction (XRD) patterns were obtained at room temperature from 5 to 90° 2θ with a Bruker-AXS D8 Advance X-ray Diffractometer setup using Co-Kα<sub>1,2</sub> radiation. The average Ni<sub>3</sub>(NO<sub>3</sub>)<sub>2</sub>(OH)<sub>4</sub>, NiO and Ni crystallite sizes were calculated according to the Scherrer equation using the most intense peaks at 2θ = 14.9, 50.8, and 52.2°, respectively. Low-angle diffraction patterns (0.5–5° 2θ) were recorded using a zero-background Si sample holder obtained from Bruker-AXS. For in situ XRD experiments, the diffractometer was equipped with an Anton-Paar XRK reaction chamber. Portions of sample S/D (~20 mg) were heated at a rate of 1 °C min<sup>-1</sup> to 248 °C in either air flow or in 5% v/v H<sub>2</sub>/He flow (100 mL min<sup>-1</sup>) and kept at 248 °C till decomposition had completed. In situ XRD patterns were recorded from 10 to 65° 2θ. Scanning transmission electron microscopy (STEM) images were obtained using a Tecnai 20 microscope operating at 200 kV and equipped with a High-Angle Annular Dark-Field (HAADF) detector. HAADF-STEM tilt series were obtained by recording images from -70° to +65° with 1° intervals. For cryo-STEM a Gatan cryoholder Model 626 was used, and the freshly impregnated sample was cooled down to -196 °C with liquid N<sub>2</sub>.

Thermogravimetric analysis (TGA) was carried out using a Perkin-Elmer Pyris 1 apparatus. Typically a quantity of 5 mg sample was heated from room temperature to 500 °C (ramp = 5 °C min<sup>-1</sup>) and an air, Ar, or 5% v/v H<sub>2</sub>/Ar gas flow of 100 mL min<sup>-1</sup>. During the TGA experiments mass spectra of the gaseous products in the off gas were simultaneously recorded with a Pfeiffer Omnistar quadrupole mass spectrometer. The m/z values (m = molar mass of X<sup>z+</sup> ion, z = charge of the ion) for which the ion currents were recorded are: 14, 15, 16, 17, 18, 28, 30, 32, 44, 46, 62, and 63.

(37) Jaroniec, M.; Kruk, M.; Olivier, J. P.; Koch, S. *Stud. Surf. Sci. Catal.* **2000**, *128*, 71–80.

(38) Barrett, E. P.; Joyner, L. S.; Halenda, P. P. *J. Am. Chem. Soc.* **1951**, *73*, 373–380.

(39) Harkins, W. D.; Jura, G. *J. Am. Chem. Soc.* **1944**, *66*, 1366–1373.

(40) Kruk, M.; Jaroniec, M.; Sayari, A. *Langmuir* **1997**, *13*, 6267–6273.

(41) Lippens, B. C.; De Boer, J. H. *J. Catal.* **1965**, *4*, 319–323.

(36) Van Leeuwen, P. W. N. M.; Groeneveld, W. L. *Inorg. Nucl. Chem. Lett.* **1967**, *3*, 145–146.

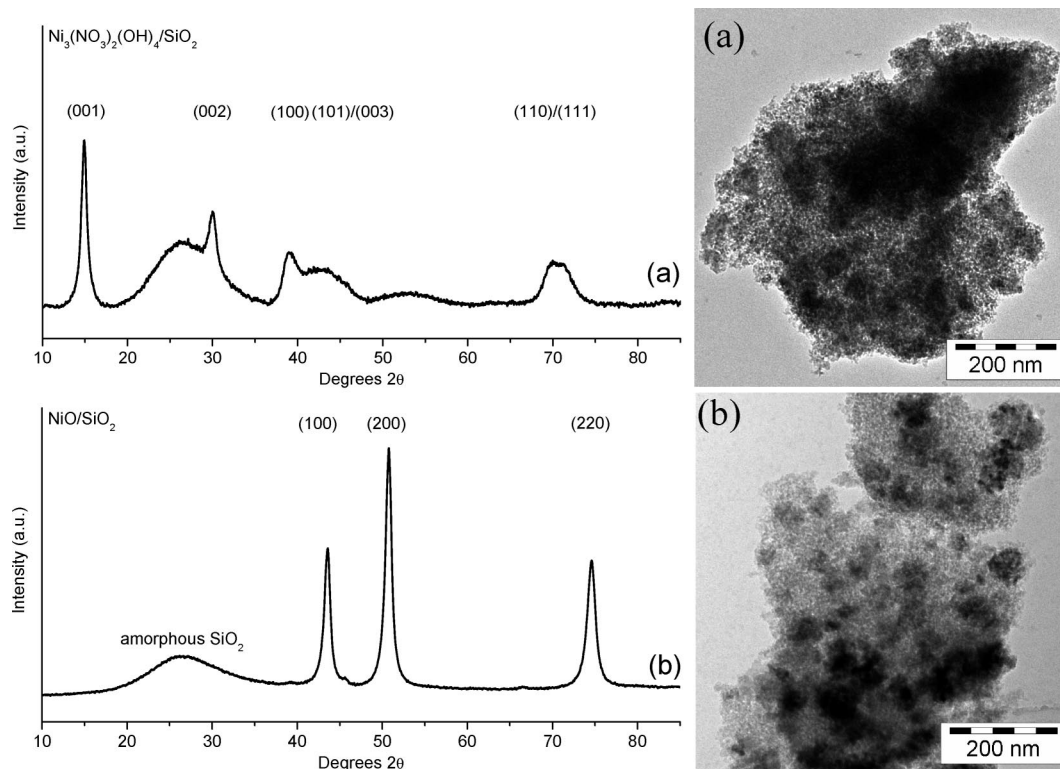


**Figure 1.** XRD patterns and TEM images of silica gel supported (a) sample G/D obtained after impregnation and drying and (b) sample G/D-C obtained after subsequent calcination.

**Table 1.** Overview of Thermal Treatments and XRD and STEM Results of Ni/SiO<sub>2</sub> Samples

thermal treatments <sup>a</sup>		nickel phase	loading (wt %)	size (nm)	
				<i>d</i> <sub>XRD</sub>	<i>d</i> <sub>STEM</sub>
Silica Gel Samples					
G/D	drying	Ni <sub>3</sub> (NO <sub>3</sub> ) <sub>2</sub> (OH) <sub>4</sub>	39	12	
G/D-C	drying/calcination	NiO	28	15	27–73
G/D-C-R	drying/calcination/reduction	Ni	23	17	10–35
G/D-R	drying/reduction	Ni	23	4	3–8
SBA-15 Samples					
S/D	drying	Ni <sub>3</sub> (NO <sub>3</sub> ) <sub>2</sub> (OH) <sub>4</sub>	34	9	
S/D-C	calcination	NiO	24	10	10–35
S/D-C-R	drying/calcination/reduction	Ni	20	12	7–25
S/D-C <sub>S</sub>	drying/calcination (stagnant air)	NiO	24	25	50–200
S/D-C <sub>NC</sub>	drying/calcination (natural convection)	NiO	24	11	20–100
S/D-R	drying/reduction	Ni	20	3 <sup>b</sup>	3–6
S/D-C <sub>air</sub>	drying/calcination <sup>c</sup>	NiO	24	9	10–40
S/D-C <sub>He</sub>	drying/heat treatment in He <sup>c</sup>	NiO	24	7	11–26
S/D-C <sub>anh</sub>	drying/calcination (dry air)	NiO	9	8	10–25
S/D-C <sub>H2O</sub>	drying/heat treatment 15 vol % H <sub>2</sub> O/He <sup>c</sup>	NiO	24	6	6–10
S/D-C <sub>NO2</sub>	drying/heat treatment 10/3 vol % NO <sub>2</sub> /O <sub>2</sub> /He <sup>c</sup>	NiO	24	16	20–90

<sup>a</sup> All drying treatments were carried out in stagnant air, whereas the following heat treatments were done under plug-flow conditions with a GHSV of 12 000 h<sup>-1</sup> unless otherwise indicated. <sup>b</sup> Underestimated size due to reoxidation of sample prior to XRD analysis. <sup>c</sup> A GHSV of 6666 h<sup>-1</sup> was used.

## Results and Discussion

First the impregnation and drying steps in the preparation of conventional Ni/SiO<sub>2</sub> catalysts were studied using silica gel powder as support. After incipient wetness impregnation with an aqueous Ni(NO<sub>3</sub>)<sub>2</sub>·6H<sub>2</sub>O solution (4.2 M) the sample was dried in air at 120 °C to yield a light-green product that was labeled G/D. XRD results (Figure 1a) showed that nickel nitrate hydroxide with composition Ni<sub>3</sub>(NO<sub>3</sub>)<sub>2</sub>(OH)<sub>4</sub> had formed. Formation of these so-called basic nitrates upon heating of Ni(NO<sub>3</sub>)<sub>2</sub>·6H<sub>2</sub>O has been described<sup>42,43</sup> and their structure resembles that of Ni(OH)<sub>2</sub>. Line-broadening analysis

of the (001) diffraction line showed that the crystallites had an average size of 12 nm. The crystal phases and average crystallite sizes found with XRD for all samples are summarized in Table 1 together with the particle size distributions derived from STEM results.

Calcination at 450 °C of the dried impregnate G/D yielded a gray product designated G/D-C with a NiO/SiO<sub>2</sub> loading of 28 wt %. Its diffraction pattern (Figure 1b) demonstrated that the crystalline Ni<sub>3</sub>(NO<sub>3</sub>)<sub>2</sub>(OH)<sub>4</sub> phase had completely decomposed during the thermal treatment to form NiO crystals of 15 nm on average. The gray color of the sample

(42) Gallezot, P.; Prettre, M. *Bull. Soc. Chim. Fr.* **1969**, 2, 407–411.

(43) Estellé, J.; Salagre, P.; Cesteros, Y.; Serra, M.; Medina, F.; Sueiras, J. E. *Solid State Ionics* **2003**, 156, 233–243.

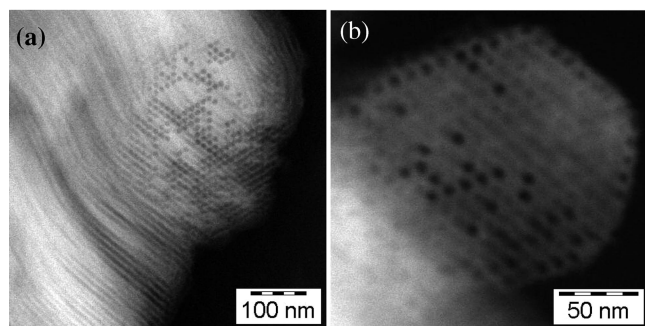


**Figure 2.** Cryo HAADF-STEM images of SBA-15 that was pore volume impregnated with an aqueous  $[\text{Ni}(\text{OH})_2]_6(\text{NO}_3)_2$  solution and frozen to  $-196^\circ\text{C}$ ; the images show that a significant number of pores (dark) remained empty upon impregnation.

is most likely due to some deviation from ideal 1:1 stoichiometry of the NiO. Taking into account the density increase upon conversion of  $\text{Ni}_3(\text{NO}_3)_2(\text{OH})_4$  ( $\sim 3.5 \text{ g cm}^{-3}$ ) into NiO ( $6.7 \text{ g cm}^{-3}$ ), and assuming no change in crystal geometry, the observed increase from 12 to 15 nm was unexpected. This suggested that some sintering had taken place during calcination. Both dried (G/D) and air calcined (G/D-C) samples were characterized using STEM, and typical images are depicted in images a and b in Figure 1, respectively. The image of the dried sample G/D demonstrated that it is difficult to distinguish the  $\text{Ni}_3(\text{NO}_3)_2(\text{OH})_4$  precursor from the support. This is due to both the low contrast difference between precursor and support and the heterogeneity of the support. It was not possible to derive an average  $\text{Ni}_3(\text{NO}_3)_2(\text{OH})_4$  particle size, or to determine its distribution over the support. Figure 2b also shows that after calcination, limited information could be obtained despite the enhanced contrast of the NiO over the  $\text{SiO}_2$  support. NiO domains could be distinguished, and a rough estimate provided 27–73 nm for their size range, which also suggested that severe sintering had taken place.

Next, an ordered mesoporous  $\text{SiO}_2$  (i.e., SBA-15) was employed to address the impact of each step in the preparation on the final Ni metal dispersion and distribution over the support. After incipient wetness impregnation of SBA-15 with an aqueous 4.2 M  $[\text{Ni}(\text{OH})_2]_6(\text{NO}_3)_2$  solution, the fresh impregnate was frozen to  $-196^\circ\text{C}$  with liquid  $\text{N}_2$ , and was studied with cryo-STEM to determine the distribution of precursor solution over the SBA-15 support particles. To our best knowledge, monitoring the precursor solution distribution inside SBA-15 particles with TEM has not been reported before. Two typical cryo HAADF-STEM images are depicted in Figure 2. With this technique, the precursor phase can be clearly discriminated from the  $\text{SiO}_2$  support because of the Z-contrast<sup>44</sup> and the ordered structure of the support. The electron micrographs show the hexagonal array of mesopores of SBA-15, and incomplete filling of these pores with precursor solution as a large number of empty pores (dark) were observed. Subsequently, fresh impregnate was dried for 12 h at  $120^\circ\text{C}$  in static air and again studied

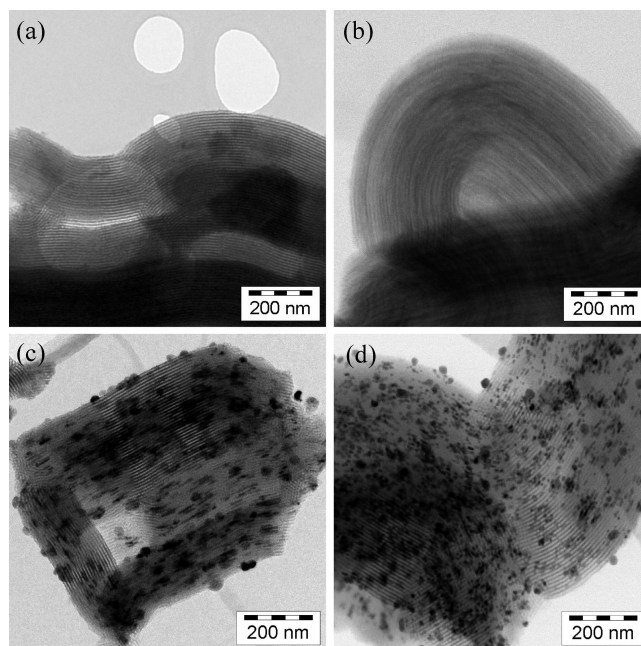


**Figure 3.** STEM images of (a) pristine SBA-15, (b) dried impregnated  $\text{Ni}_3(\text{NO}_3)_2(\text{OH})_4/\text{SBA-15}$  sample S/D, (c)  $\text{NiO}/\text{SBA-15}$  sample S/D-C after subsequent calcination in air, and (d)  $\text{Ni}/\text{SBA-15}$  sample S/D-C-R after reduction.

with (HAADF)-STEM. Images a and b in Figure 3 show STEM images of pristine SBA-15 and the dried impregnate labeled S/D, respectively. The STEM analysis indicated that  $\text{Ni}_3(\text{NO}_3)_2(\text{OH})_4$  was only present inside the mesopores as no agglomerates or particles of precursor were found at the exterior surface of the SBA-15 particles. This could be explained by considering that the capillary pressure in the mesopores is much higher than that in the macropores present between the SBA-15 particles. Consequently, precursor solution is readily sucked into the mesopores upon impregnation. In line with this, Yue et al. recently demonstrated that migration of  $\text{Ni}(\text{NO}_3)_2 \cdot 6\text{H}_2\text{O}$  into the mesopores of SBA-15 takes place upon heating of a physical mixture of these two components above the melting point of the nitrate ( $\sim 60^\circ\text{C}$ ).<sup>45,46</sup> Hence, upon reaching a temperature higher than  $60^\circ\text{C}$  during the drying treatment, initially externally deposited  $\text{Ni}(\text{NO}_3)_2 \cdot 6\text{H}_2\text{O}$  migrates into the mesopores explaining the absence of precursor particles at the exterior surface in the dried impregnate. Additional HAADF-STEM tilt series of individual SBA-15 particles of the dried impregnate S/D confirmed the absence of precursor outside the mesopores, but also indicated their incomplete filling. In Figure 4, HAADF-STEM images are given that were collected at different angles and extracted from a typical tilt series. In particular the image recorded at  $-61^\circ$  shows that not all of the pores of the SBA-15 particle had been filled upon impregnation and drying. As a rough estimate we concluded from the STEM results that 30–60% of the mesopores appeared empty after impregnation and drying. The presence of unfilled pores with ordered mesoporous silica supported metal (oxide) catalysts has been observed

(44) Thomas, J. M.; Midgley, P. A.; Yates, T. J. V.; Barnard, J. S.; Raja, R.; Arslan, I.; Weyland, M. *Angew. Chem., Int. Ed.* **2004**, *43*, 6745–6747.

(45) Yue, W.; Zhou, W. *Chem. Mater.* **2007**, *19*, 2359–2363.

(46) Yue, W.; Hill, A. H.; Zhou, W. *Chem. Commun.* **2007**, 2518–2520.

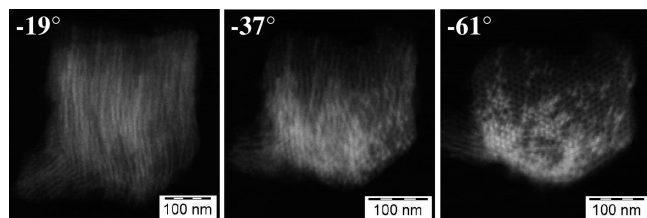


**Figure 4.** HAADF-STEM images of dried impregnated S/D recorded at different angles and showing the incomplete filling of all of the pores with precursor (bright spots/lines).

by others too.<sup>47,48</sup> Since the hydroxyl density of SBA-15 is low ( $\sim 1\text{--}2\text{ OH nm}^{-2}$ )<sup>49,50</sup> compared to that of conventional silicas ( $4\text{--}6\text{ OH nm}^{-2}$ )<sup>51</sup> the wetting could be significantly affected by small changes in the local silanol density in a single pore. Hence, we propose that the incomplete filling of pores originates in nonuniform wetting by the impregnation solution. XRD showed again that the dried impregnate contained  $\text{Ni}_3(\text{NO}_3)_2(\text{OH})_4$ , but now with an average crystallite size of 9 nm. This is in good agreement with the average mesopore diameter of 9 nm of the support as determined by  $\text{N}_2$ -physisorption, and indicated that the pore walls had confined the crystal growth. This is in line with the STEM observations that precursor was found inside the mesoporous channels of SBA-15 only.

In Figure 5, the  $\text{N}_2$ -physisorption isotherms of pristine SBA-15 and samples S/D, S/D-C, and S/D-C-R are shown. Details of the textural properties derived from these isotherms are given in Table 2 together with those obtained for the other samples used in this study. The physisorption results were corrected for the contribution of precursor to the total weight of the sample and expressed per gram of  $\text{SiO}_2$ . The isotherm of the unloaded SBA-15 is typical for this material: a high onset at low relative pressures originating from the intrawall microporosity, and hysteresis at higher values because of the mesoporous channels. The small relative pressure region ( $p/p_0 = 0.69\text{--}0.71$ ) in which the single-step capillary condensation took place is a consequence of the uniform mesopore diameter of 9 nm. Impregnation of the support with aqueous  $[\text{Ni}(\text{OH}_2)_6](\text{NO}_3)_2$  solution followed by drying (Table 2, sample S/D) led to a decrease in total pore volume ( $V_{\text{tot,exp}}$ ) to  $0.47\text{ mL g}^{-1}\text{ SiO}_2$ , while a decrease to  $0.63\text{ mL g}^{-1}\text{ SiO}_2$  was expected ( $V_{\text{tot,calc}}$ ). The desorption branch of the isotherm contained a new feature in the relative pressure region of 0.45 to 0.6, namely delayed closure of the hysteresis loop. Because the adsorption branch did not show capillary condensation effects at these values, this feature could be associated with ink-bottle type pores<sup>32–34</sup> formed by filling of the mesopores of SBA-15 with  $\text{Ni}_3(\text{NO}_3)_2(\text{OH})_4$ . The partially blocked mesopore volume ( $V_{\text{meso,bl}}$ ) was found to be 19% of the total accessible

mesoporosity. Since the porosity of sample S/D was significantly lower than expected, we investigated the stability of the ordered structure of the SBA-15 support upon impregnation and drying. We compared the long-range order of the mesopores of sample S/D to that of pristine SBA-15 with low-angle XRD (Figure 6). Both patterns contain three well-resolved diffraction lines that could be indexed as the (100), (110) and (200) lattices of a unit cell with a  $p6mm$  hexagonal symmetry, which is typical for SBA-15.<sup>31</sup> Taking a closer look at the  $2\theta$  region from 2.2 up to 4.0, for example as shown in the insert for sample S/D, the (210) and (300) diffraction lines could be identified too. Especially the presence of the latter diffractions in both patterns, and the relatively high ratio between the (110) and (200), and the (100) lines demonstrated on the one hand that high-quality SBA-15 was synthesized, and on the other hand that the impregnation and drying steps had not significantly affected the long-range order of the mesopores. Hence, the decreased porosity is presumably due to the formation of inaccessible domains in the sample.

XRD results of the air calcined sample S/D-C (Table 1) showed that NiO crystallites with an average size of 10 nm had formed. Similar to the results found with silica gel this suggests sintering as the crystal size did not decrease as expected from the density increase upon conversion of  $\text{Ni}_3(\text{NO}_3)_2(\text{OH})_4$  into NiO. STEM analysis (Figure 3c) demonstrated that the precursor phase had severely sintered upon calcination in air. Two types of NiO particles could be distinguished. The first type consisted of large NiO particles of 10–35 nm localized at the exterior surface of the SBA-15 particles, whereas the second type had not been transported over such large distances and was retained inside the mesopores. The latter particles appeared to have adopted a rod-like geometry suggesting that the diameter of these particles was restricted by the pore walls. Since the mesopores of SBA-15 are microporous, migration could have been influenced by the presence of these pores.  $\text{N}_2$ -physisorption (Figure 5 and Table 2) showed that the total porosity had increased compared to sample S/D as expected because of the decreased volume and the location of the NiO phase. In addition, the intrawall micro porosity was close to its original value. Finally, the quantity of  $\text{N}_2$  released from ink-bottle type pores during desorption had significantly increased from 19% to 75% going from sample S/D to sample S/D-C due to the rodlike NiO particles.

The final step in the preparation was carried out by reducing the SBA-15 supported NiO in a diluted stream of 5% v/v  $\text{H}_2/\text{Ar}$  to Ni metal (sample S/D-C-R). XRD analysis disclosed that the catalyst had an average Ni crystallite size of 12 nm, which is a slight underestimation as the outer-shell of the particles had been reoxidized during passivation. STEM results (Figure 3d) demonstrated that little had changed with respect to the distribution of the active phase over the support, and particles with sizes ranging from 7 to 25 nm were observed.  $\text{N}_2$ -physisorption demonstrated that the microporosity decreased, whereas the mesoporosity increased. The percentage of the ink-bottle type of pores (69%) had hardly changed during reduction. The total pore volume was close to its expected value. Finally, comparison

(47) Moreno, S. M.; Weyland, M.; Midgley, P. A.; Bengoa, J. F.; Cagnoli, M. V.; Gallegos, N. G.; Alvarez, A. M.; Marchetti, S. G. *Micron* **2006**, *37*, 52–56.

(48) Imperor-Clerc, M.; Bazin, D.; Appay, M-D.; Beaunier, P.; Davidson, A. *Chem. Mater.* **2004**, *16*, 1813–1821.

(49) Jentys, A.; Kleestorfer, K.; Vinek, H. *Microporous Mesoporous Mater.* **1999**, *27*, 321–328.

(50) Ek, S.; Root, A.; Peussa, M.; Niinistö, L. *Thermochim. Acta* **2001**, *379*, 201–212.

(51) Zhuravlev, L. T. *Langmuir* **1987**, *3*, 316–318.

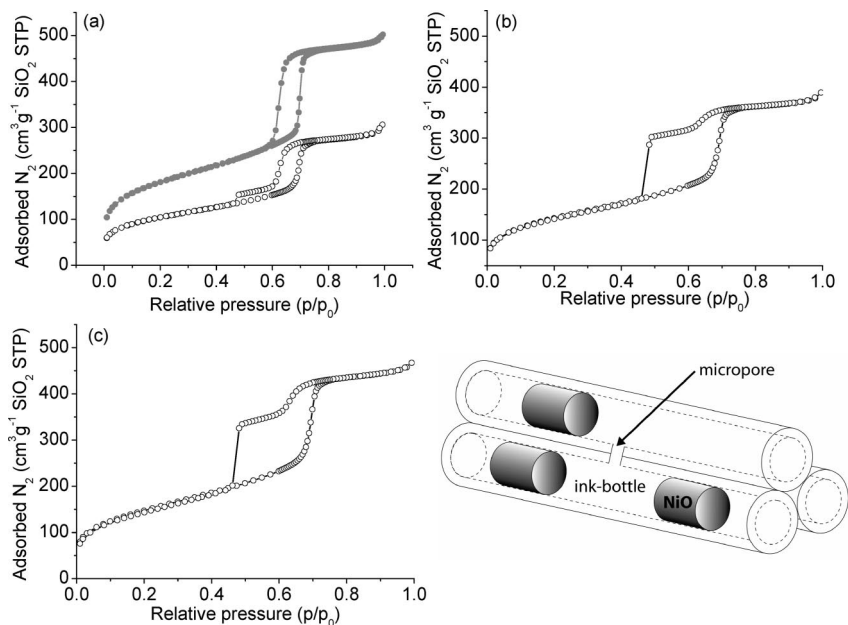


**Figure 5.**  $N_2$  physisorption isotherms of (a) pristine SBA-15 (grey) and dried impregnate S/D, (b) air calcined product S/D-C, (c) reduced sample S/D-C-R, and a schematic representation of the ink-bottle pores formed by the rodlike NiO particles inside the mesopores with the intrawall micropores as pore neck.

**Table 2.**  $N_2$ -Physisorption Results of SBA-15-Supported Ni Samples

sample	surface area ( $m^2 g^{-1} SiO_2$ )		porosity ( $cm^3 g^{-1} SiO_2$ )					
	$S_t^a$	$S_{t,ext}^b$	$V_{tot, calc}^c$	$V_{tot, exp}^d$	$V_{micro}^e$	$V_{meso}^f$	$V_{meso,bl}^g$	(%)
SBA-15	516	38	0.78	0.78	0.05	0.68	0.00	0
S/D	293	33	0.63	0.47	0.01	0.42	0.08	19
S/D-C	409	31	0.73	0.66	0.06	0.56	0.42	75
S/D-C-R	487	45	0.75	0.72	0.01	0.67	0.46	69
S/D-R	474	40	0.75	0.64	0.03	0.57	0.24	42
S/D-C <sub>S</sub>	388	33	0.73	0.65	0.04	0.56	0.15	27
S/D-C <sub>Nc</sub>	375	32	0.73	0.61	0.05	0.53	0.24	45
S/D-C <sub>air</sub>	384	30	0.73	0.60	0.06	0.50	0.40	80
S/D-C <sub>He</sub>	442	34	0.73	0.59	0.03	0.51	0.29	57
S/D-C <sub>anh</sub>	304	23	0.76	0.44	0.02	0.39	0.30	77
S/D-C <sub>H<sub>2</sub>O</sub>	376	34	0.73	0.53	0.04	0.46	0.21	46
S/D-C <sub>NO<sub>2</sub></sub>	280	24	0.73	0.44	0.03	0.38	0.25	66

<sup>a</sup> Mesopore surface area determined using t-method. <sup>b</sup> External surface area calculated using t-method. <sup>c</sup> Expected total pore volume based on contribution of Ni precursor to volume decrease. <sup>d</sup> Total pore volume based on amount  $N_2$  adsorbed at  $p/p_0 = 0.995$ . <sup>e</sup> Micropore volume calculated using NL-DFT. <sup>f</sup> Mesopore volume calculated using NL-DFT. <sup>g</sup> Partially blocked mesopore volume calculated from desorption branch (see Experimental Section for details).

of the pore size distribution plots (not depicted) obtained from the adsorption branch of the isotherms of each dried, calcined and reduced sample with that of pristine SBA-15 demonstrated that the impregnation and drying technique, and thermal treatments used to convert the precursor into the desired Ni metal had little effect on the pore diameter of the accessible mesopores of SBA-15.

After studying the SBA-15 products obtained after each step in the preparation, we could unambiguously conclude that the calcination treatment in air had the most detrimental effect on the final metal dispersion and distribution over the silica support.

Results obtained with a catalyst prepared via a synthesis route that modified this step, previously used by Soled et al.<sup>52</sup> to improve the performance of Co-based catalysts in the Fischer–Tropsch synthesis, further supported our findings.

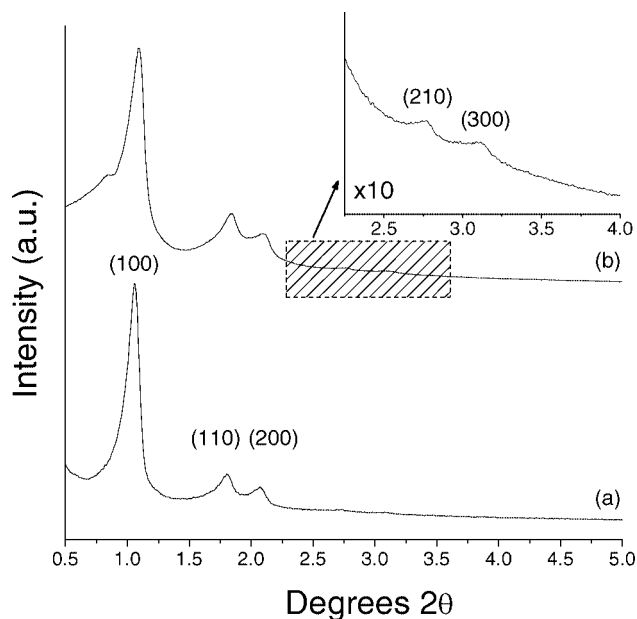


**Figure 6.** Low-angle XRD patterns of (a) pristine SBA-15 and (b)  $Ni_3(NO_3)_2(OH)_4/SBA-15$  sample S/D obtained after impregnation and drying.

Dried impregnate sample S/D was thermally treated in a diluted stream of 5% v/v  $H_2/Ar$  to obtain a Ni/SBA-15 catalyst labeled S/D-R. XRD showed an average Ni crystal size of 3 nm had formed. From this it is likely that the Ni crystallites originally had a size of 4 to 5 nm. STEM results (Figure 7) confirmed that the Ni particles were small (3 to 6 nm) and rather homogeneously distributed throughout the mesopores of SBA-15. No Ni particles were found at the external surface of the SBA-15 particles. Thus, the homogeneous distribution over the support after drying with

(52) Soled, S. L.; Iglesia, E.; Fiato, R. A.; Baumgartner, J. E.; Vroman, H.; Miseo, S. *Top Catal.* **2003**, *26*, 101–109.

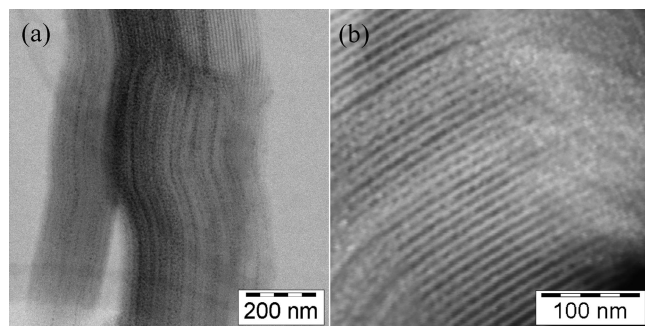


**Figure 7.** (a) STEM and (b) HAADF-STEM images of Ni/SBA-15 sample S/D that was heat treated in a 5% v/v H<sub>2</sub>/Ar flow to yield sample S/D-R.

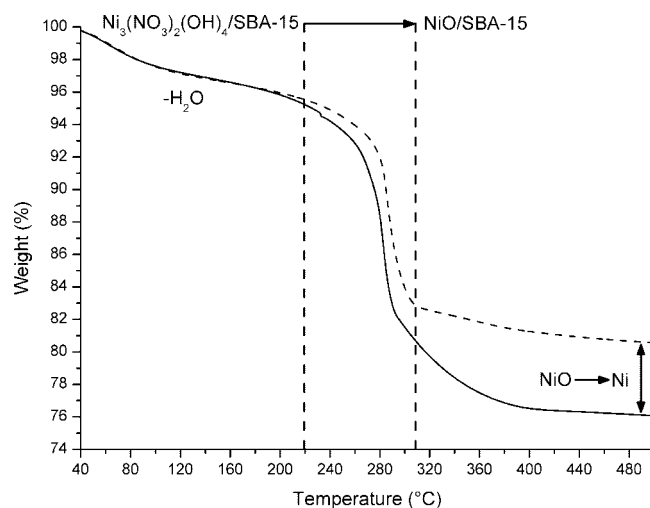


**Figure 8.** TGA results obtained during calcination in air flow (broken line) or heat treatment in 5% v/v H<sub>2</sub>/Ar flow (black line) of dried impregnate S/D.

sample S/D could be retained by avoiding a separate air calcination treatment. N<sub>2</sub>-physisorption showed that the degree of pore blocking was significantly lower (42%) than for the sample S/D-C-R (69%) prepared via the route including the calcination step. Also the total porosity was lower compared to that of sample S/D-C-R, partly due to the larger fraction of Ni particles inside the mesopores.

Because the air calcination step had clearly proven to have an unfavorable impact on the final dispersion of the catalyst we studied this step in more detail. With TGA coupled with mass-spectrometry (MS) we monitored the weight loss and the type of gaseous products formed during air calcination of SBA-15 supported Ni<sub>3</sub>(NO<sub>3</sub>)<sub>2</sub>(OH)<sub>4</sub>. A small quantity (~10 mg) of sample S/D was calcined using a heating rate of 5 °C min<sup>-1</sup>. The measured weight loss curve is shown in Figure 8. The weight loss starting at 50 °C was predominantly caused by the removal of physisorbed water from the surface of the SBA-15 support. Other TGA and solid-state <sup>1</sup>H-MAS NMR spectroscopy studies have shown that the removal of physisorbed water is completed at approximately 200 °C.<sup>50,53</sup> At higher temperatures dehydration is predominantly caused by dehydroxylation of the SiO<sub>2</sub> surface, although in the Ni<sub>3</sub>(NO<sub>3</sub>)<sub>2</sub>(OH)<sub>4</sub>/SBA-15 system some de-

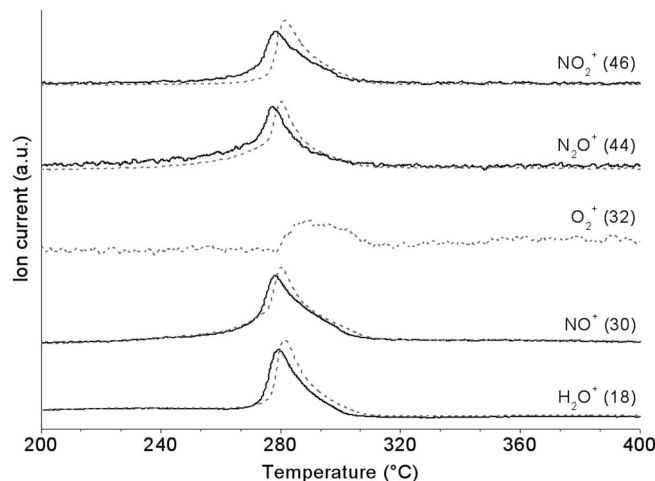


**Figure 9.** MS results of the off gas during calcination in air flow (black lines) or heat treatment in Ar flow (grey lines) of dried impregnate S/D.

hydration of the precursor phase could take place too. More extensive weight loss started gradually at ~220 °C, which rapidly increased at higher temperatures and was completed at ~310 °C. The weight loss of 13% in this range matched the expected loss due to conversion of the Ni<sub>3</sub>(NO<sub>3</sub>)<sub>2</sub>(OH)<sub>4</sub> into NiO. On the one hand, this indicates that decomposition had completed at 310 °C, and on the other hand it showed that during the drying treatment of the impregnate, Ni(NO<sub>3</sub>)<sub>2</sub>·6H<sub>2</sub>O had been entirely converted into Ni<sub>3</sub>(NO<sub>3</sub>)<sub>2</sub>(OH)<sub>4</sub>. Further heating of the sample to the final temperature of 500 °C led to a gradual weight loss of 2% due to dehydroxylation of the support. Experiments with a heating rate of 1 °C min<sup>-1</sup> showed similar results, although in this case decomposition was already complete at 280 °C.

The MS signals of gaseous products that were found to evolve during calcination have been plotted as a function of the temperature (Figure 9). It should be noted that signals due to the mass fractions 15 (NH<sup>+</sup>) and 62/63 (NO<sub>3</sub><sup>+</sup>/HNO<sub>3</sub><sup>+</sup>) typical for NH<sub>3</sub> and HNO<sub>3</sub>, respectively, were not observed. The observed mass fraction 18 (H<sub>2</sub>O<sup>+</sup>) originated from H<sub>2</sub>O. The presence of the NO<sub>2</sub><sup>+</sup> fraction (*m/z* = 46) demonstrated that a significant amount of NO<sub>2</sub> evolved. Correction of the NO<sub>2</sub><sup>+</sup> (37%) and NO<sup>+</sup> (100%) intensities for their relative abundance indicated that the latter fraction also originated from NO<sub>2</sub>. Finally, *m/z* = 44 could be associated with both CO<sub>2</sub> and N<sub>2</sub>O. With GC analysis (not shown) of the gaseous products we established that N<sub>2</sub>O and not CO<sub>2</sub> evolved. Recently, Małeckı et al. reported for bulk Ni(NO<sub>3</sub>)<sub>2</sub>·6H<sub>2</sub>O that N<sub>2</sub>O contributes to 5–8% of the total nitrogen content released during decomposition.<sup>54</sup> Although our MS results do not allow quantification, they indicated that the concentration of N<sub>2</sub>O was much lower than that of NO<sub>2</sub>. Next to H<sub>2</sub>O and NO<sub>2</sub>, O<sub>2</sub> is expected to form. However, the relatively small amounts of this compound could not be detected since decomposition of the SBA-15 supported Ni<sub>3</sub>(NO<sub>3</sub>)<sub>2</sub>(OH)<sub>4</sub> was carried out in air. Therefore, we also decomposed sample S/D through heating in an argon atmosphere and recorded MS spectra (Figure 9). In this case next to the expected H<sub>2</sub>O, N<sub>2</sub>O and NO<sub>2</sub> products, O<sub>2</sub> (*m/z*

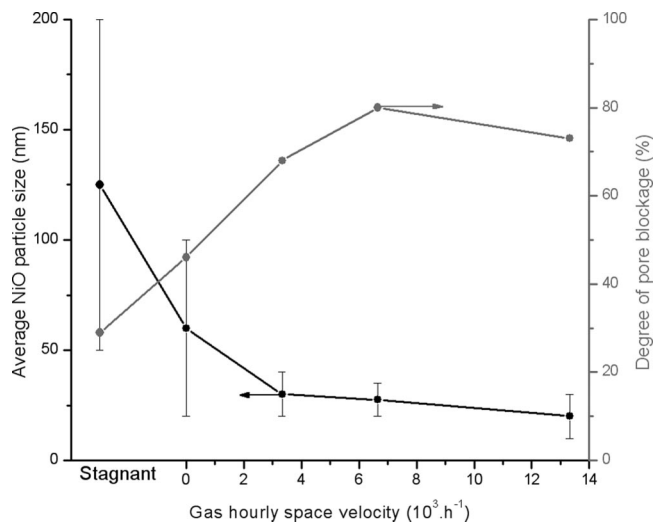
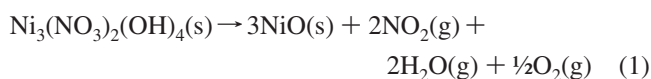


**Figure 10.** Influence of GHSV during air calcination; the black dots and bars indicate the average and spread in NiO particles found outside the mesopores of SBA-15, respectively. The grey dots indicate the degree of mesopore blockage by NiO present inside the mesopores.

= 32) was detected albeit in low concentrations. Hence, the decomposition products of supported  $\text{Ni}_3(\text{NO}_3)_2(\text{OH})_4$  can be largely accounted for by eq 1



To study the impact of the gaseous decomposition products on the transformation of  $\text{Ni}_3(\text{NO}_3)_2(\text{OH})_4$  into NiO a series of experiments was carried out using different gas atmospheres and calcination conditions. First, the impact of the concentration of decomposition products was investigated by calcination in air flow of sample S/D using different GHSVs during heating in a plug-flow reactor. In Figure 10, the impact of the GHSV on the average and spread in NiO particle sizes found at the exterior surface of the SBA-15 particles as determined by STEM (left axis) is given. Also included are the results for sample S/D- $\text{C}_\text{S}$  that was prepared by calcination in stagnant air. The results show that going from calcination in stagnant air to natural convection (GHSV =  $0 \text{ h}^{-1}$ ) led to decrease of a factor of 2 in the average NiO particle size (125 to 60 nm). Moreover, the spread in NiO particle sizes had significantly narrowed. Maintaining a GHSV of  $3,333 \text{ h}^{-1}$  resulted in a similar NiO particle size reduction. Although increasing the GHSV resulted in a further decrease of the average particle size, the spread in the particle sizes remained rather constant. Also shown in Figure 10 (right axis) is the effect of the GHSV on the degree of mesopore blockage by the rodlike NiO particles that retained inside the SBA-15 particles as calculated from  $\text{N}_2$ -physisorption. The results confirmed the STEM finding that upon increase of the GHSV precursor mobility to the external surface of the support particles reduced as the degree of pore blockage increased as a consequence of a larger degree of retention of NiO in the mesopores. Thus, we could conclude that the decomposition products (i.e., primarily  $\text{H}_2\text{O}$ ,  $\text{NO}_2$  and  $\text{O}_2$ ) play a crucial role in the sintering and redistribution

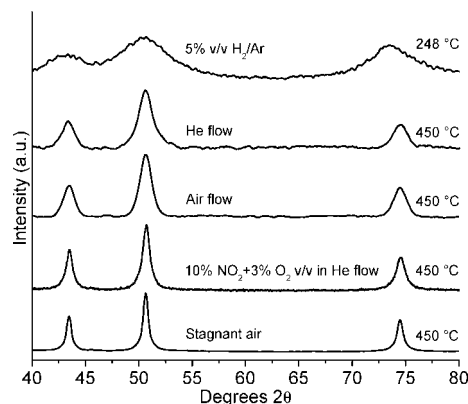


**Figure 11.** XRD patterns of sample S/D after thermal treatment at temperatures and gas atmospheres as indicated.

of NiO. Although mobility could be significantly reduced by applying a GHSV  $> 3000 \text{ h}^{-1}$ , the intraporous migration leading to pore blocking is apparent even at the highest GHSV indicating significant sintering.

Subsequently, we studied the effects of the individual products, namely  $\text{O}_2$ ,  $\text{H}_2\text{O}$  and  $\text{NO}_2$  by variation of their concentration during the decomposition of sample S/D at a GSHV of  $6666 \text{ h}^{-1}$ . The role of  $\text{O}_2$  was inferred from comparison of the air calcined sample to thermal decomposition of sample S/D in a He flow. The sample was designated S/D- $\text{C}_\text{He}$ . An average crystal size of 7 nm was found from XRD, which was significantly smaller than had been found with an air flow (10 nm). Comparison of the pattern with that of the air calcined sample S/D-C (Figure 11) revealed that the NiO diffraction lines of sample S/D- $\text{C}_\text{He}$  originated from a bimodal crystal size distribution, suggesting also the presence of crystallites smaller than 7 nm. STEM analysis (Figure 12a) showed that again NiO particles had been deposited inside the mesoporous channels as well as on the external surface of the support particles. However, the size of the latter particles had significantly decreased to 11–26 nm. STEM analysis also indicated that less NiO had migrated out of the mesopores. The morphology of the majority of particles inside these pores was similar to observed in air, namely rodlike. However, smaller particles with a spherical geometry were occasionally observed too.  $\text{N}_2$ -physisorption results showed that significant pore blocking (57%) took place due to the rodlike particles. Thus, the results obtained with He indicate that exclusion of  $\text{O}_2$  from the atmosphere limits precursor mobility during decomposition.

Next, the impact of  $\text{H}_2\text{O}$  was investigated by calcination in dry air of a SBA-15 supported anhydrous  $\text{Ni}(\text{NO}_3)_2$  sample, and by thermally treating sample S/D in He containing 15% v/v of  $\text{H}_2\text{O}$  vapor. The obtained products were labeled S/D- $\text{C}_\text{anh}$  and S/D- $\text{C}_\text{H}_2\text{O}$ , respectively. It should be noted that the NiO loading of sample S/D- $\text{C}_\text{anh}$  was limited to 9 wt % due to the limited solubility of anhydrous  $\text{Ni}(\text{NO}_3)_2$  in the dry ethanol solvent. Prior to calcination the distribution of the anhydrous  $\text{Ni}(\text{NO}_3)_2$  precursor over the support was checked using HAADF-STEM and found to be similar as observed with sample S/D. Thus, not all pores had been filled with precursor, but those filled appeared to have a homogeneous distribution of precursor within the pore. After

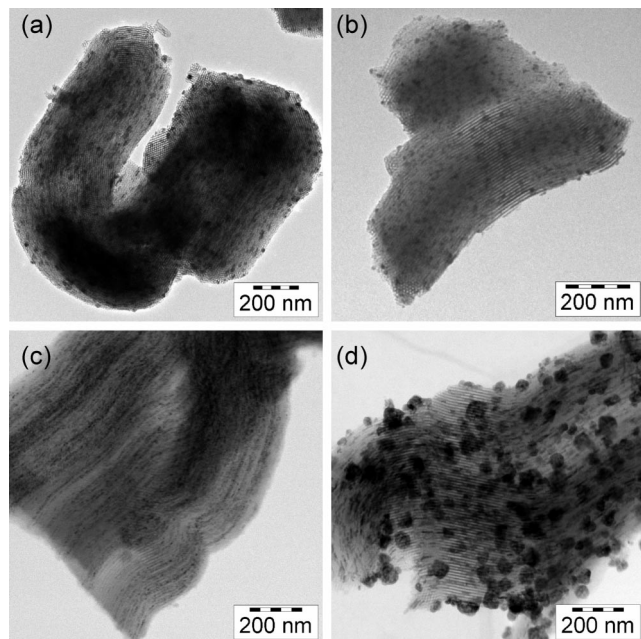


**Figure 12.** STEM images of sample S/D-C<sub>Hc</sub> obtained through thermal treatment in (a) pure He flow, (b) sample S/D-C<sub>anh</sub> heat treated in dry air, (c) sample S/D-C<sub>H2O</sub> heat treated in a 15% v/v H<sub>2</sub>O/He flow, and (d) sample S/D-C<sub>NO2</sub> that was obtained after thermal treatment in a 10/3% v/v NO<sub>2</sub>/O<sub>2</sub> in He flow.

calcination of S/D-C<sub>anh</sub> an average crystal size of 8 nm was found with XRD. NiO particles were observed at the external surface with sizes ranging from 10 to 25 nm (Figure 12b), and also rod-like NiO plugs were found nonuniformly distributed throughout the pores. N<sub>2</sub>-physorption showed that these particles blocked 77% of the mesopore volume. Hence, exclusion of H<sub>2</sub>O did not prevent sintering. Adding H<sub>2</sub>O vapor to the gas atmosphere on the other hand did show a significant impact. In Figure 12c an STEM image is included obtained for sample S/D-C<sub>H2O</sub> that was thermally treated while maintaining a relatively high H<sub>2</sub>O vapor partial pressure. The electron micrograph illustrates that addition of 15% v/v H<sub>2</sub>O vapor to He led to an inhibiting effect on precursor mobility as the pure He treated sample primarily displayed rod-like particles, whereas the H<sub>2</sub>O treated sample showed smaller and more spherical particles inside the mesopores of 6–10 nm. Using XRD line-broadening for sample S/D-C<sub>H2O</sub> an average NiO crystal size of 6 nm was found. Partly due to the smaller NiO particles, the degree of pore blocking had decreased from 57 to 46% compared with the pure He treated sample S/D-C<sub>Hc</sub>. Although the impact of H<sub>2</sub>O on the sintering process is not yet well-understood, we could derive from these results that thermal decomposition in the presence of steam slightly reduced the degree of precursor sintering and redistribution. Finally, the role of NO<sub>2</sub>/O<sub>2</sub> was studied by heating sample S/D in a flow of He that contained 10% v/v NO<sub>2</sub> and 3% v/v of O<sub>2</sub>. The obtained product was denoted S/D-C<sub>NO2</sub>, and a typical STEM image is depicted in Figure 12d. The electron micrograph demonstrated that migration outside the mesopores was severe as NiO particles of 20–90 nm were observed at the exterior surface of the support particles. Analysis of the XRD diffraction lines (Figure 11) supported the STEM observations as an average NiO crystallite size of 16 nm was found.

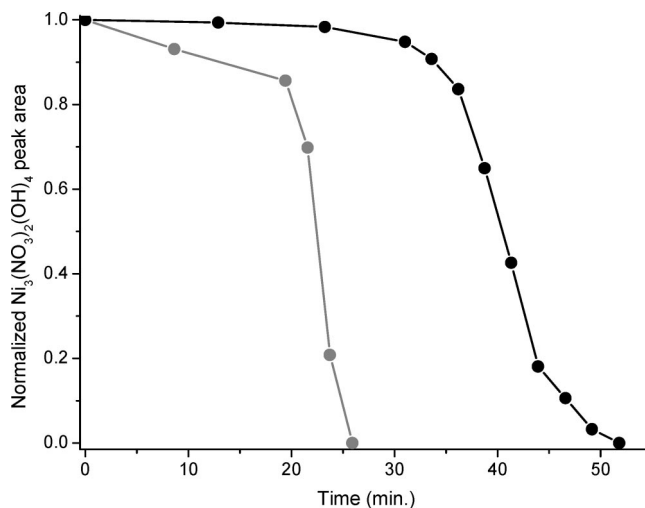


**Figure 13.** In situ XRD results obtained during decomposition of SBA-15-supported Ni<sub>3</sub>(NO<sub>3</sub>)<sub>2</sub>(OH)<sub>4</sub> into NiO at a constant temperature of 248 °C under either air flow (grey line) or 5% v/v H<sub>2</sub>/He flow (black line).

In conclusion, the results obtained for the air calcined and He treated samples indicated that O<sub>2</sub> plays a role in the sintering process. Moreover, NO<sub>2</sub> enhanced sintering too, whereas steam inhibited the precursor transport out of the pores.

We already showed that omitting the air calcination step significantly reduced the particle size of the final Ni metal phase and improved its distribution over the support (sample S/D-R, Figure 7). Therefore, we studied the impact of H<sub>2</sub> on the decomposition of Ni<sub>3</sub>(NO<sub>3</sub>)<sub>2</sub>(OH)<sub>4</sub> in more detail using in situ XRD and TGA/MS. With in situ XRD the thermal decomposition of the crystalline Ni<sub>3</sub>(NO<sub>3</sub>)<sub>2</sub>(OH)<sub>4</sub> phase in a 5% H<sub>2</sub>/He flow was monitored. Similar experiments were carried out using an air flow. The normalized peak areas of the Ni<sub>3</sub>(NO<sub>3</sub>)<sub>2</sub>(OH)<sub>4</sub> (001) diffraction line obtained during isothermal decomposition at 248 °C either in 5% v/v H<sub>2</sub>/He or an air flow have been plotted in Figure 13. Decomposition in air proceeded relatively fast, after an initial slow start, and around 90% of the Ni<sub>3</sub>(NO<sub>3</sub>)<sub>2</sub>(OH)<sub>4</sub> had decomposed within five minutes. Decomposition of the Ni<sub>3</sub>(NO<sub>3</sub>)<sub>2</sub>(OH)<sub>4</sub> in the H<sub>2</sub>/He flow was inhibited much longer than in the air flow, but after an incubation time of ~32 min decomposition of Ni<sub>3</sub>(NO<sub>3</sub>)<sub>2</sub>(OH)<sub>4</sub> started and proceeded during 20 min. Decomposition of around 90% of the Ni<sub>3</sub>(NO<sub>3</sub>)<sub>2</sub>(OH)<sub>4</sub> in H<sub>2</sub>/He atmosphere took a factor of 4 longer than in air. Both treatments led to the formation of crystalline NiO, however, the average crystallite size of the air treated sample (7 nm) was significantly larger than that of the H<sub>2</sub>/He treated sample (3 nm).

In Figure 8, the TGA curve obtained during thermal treatment of sample S/D under a stream of 5% v/v H<sub>2</sub>/Ar was plotted. The weight loss up to ~200 °C of sample S/D-R was again due to dehydration. At ~220 °C, a gradual weight loss was observed that rapidly increased at higher temperatures. This weight loss coincided with decomposition of the Ni<sub>3</sub>(NO<sub>3</sub>)<sub>2</sub>(OH)<sub>4</sub> into NiO. The next step in H<sub>2</sub>/Ar started at ~295 °C, had completed at approximately 400 °C and was accompanied with a weight loss of 4%. This weight loss corresponded with the reduction of NiO into Ni. Thus, TGA demonstrated that reduction of supported Ni<sub>3</sub>(NO<sub>3</sub>)<sub>2</sub>(OH)<sub>4</sub>

to Ni proceeded via NiO formation. The reduction of a transition metal nitrate also has been described by others to proceed via the formation of a metal oxide prior to reduction to the metal.<sup>55</sup> MS analysis of the predominant gaseous decomposition products showed that  $\text{NH}_3$  ( $m/z = 15$ ),  $\text{H}_2\text{O}$  ( $m/z = 18$ ),  $\text{NO}$  ( $m/z = 30$ ) and  $\text{N}_2\text{O}$  ( $m/z = 44$ ) were formed. However,  $\text{NO}_2$  ( $m/z = 46$ ) as well as  $\text{O}_2$  ( $m/z = 32$ ) were not detected among the gaseous decomposition products. From the effects of the individual decomposition products (vide supra) we could already conclude that  $\text{NO}_2$  and  $\text{O}_2$  decomposition products are detrimental to the final NiO dispersion. Based on the TGA and in situ XRD experiments we propose that the beneficial effect of  $\text{H}_2$  is related to its moderating effect on the decomposition rate of the  $\text{Ni}_3(\text{NO}_3)_2(\text{OH})_4$ , and its impact on the type of gaseous decomposition products formed rather than directly reducing the nitrate precursor into the Ni metal phase.

### Conclusions

The use of ordered mesoporous support SBA-15 as model system enabled us to study in detail the individual steps in the preparation of Ni/SiO<sub>2</sub> catalysts, that is impregnation, drying, calcination, and finally reduction using  $\text{Ni}(\text{NO}_3)_2 \cdot 6\text{H}_2\text{O}$  as precursor salt.

After the impregnation and drying steps not all the mesopores were filled with precursor, but in the filled pores well-dispersed  $\text{Ni}_3(\text{NO}_3)_2(\text{OH})_4$  was found.  $\text{Ni}_3(\text{NO}_3)_2(\text{OH})_4$  was found exclusively inside the mesopores and its average crystal size of 9 nm was in good agreement with the pore diameter of the mesopores of SBA-15. During the calcination

step in air severe sintering and redistribution took place, resulting in deposition of large NiO particles (10–35 nm) outside the mesopores as well as rodlike NiO plugs inside the mesopores. The degree of NiO migration to the exterior surface increased with higher concentrations of gaseous decomposition products that evolved during the formation of NiO from  $\text{Ni}_3(\text{NO}_3)_2(\text{OH})_4$ . MS results showed that these gaseous decomposition products consisted of  $\text{H}_2\text{O}$ ,  $\text{N}_2\text{O}$ ,  $\text{NO}_2$ , and  $\text{O}_2$ . We found that in particular the latter two promoted sintering and redistribution during the thermal treatment, whereas  $\text{H}_2\text{O}$  vapor was found to have an inhibiting effect on the sintering. Furthermore, we showed that sintering during  $\text{Ni}_3(\text{NO}_3)_2(\text{OH})_4$  decomposition could be avoided if carried out in the presence of  $\text{H}_2$ . With  $\text{H}_2$  formation of the  $\text{O}_2$  and  $\text{NO}_2$  decomposition products was prevented.  $\text{H}_2$  also showed to moderate the rate of  $\text{Ni}_3(\text{NO}_3)_2(\text{OH})_4$  decomposition avoiding rapid decomposition as observed in air. The 24 wt % NiO/SBA-15 samples treated in a 5% v/v  $\text{H}_2/\text{He}$  flow displayed a high NiO dispersion (crystallites of 3 nm on average) contrary to samples treated either in air or in pure He. Hence, when highly dispersed and highly loaded Ni/SiO<sub>2</sub> catalysts are desired, use of an  $\text{H}_2$ -containing atmosphere is beneficial. Previously we published similar findings with NO.<sup>56</sup> Because a mutual property of  $\text{H}_2$  and NO is the strong reactivity toward oxygen, we speculate that oxygen radicals formed upon decomposition are scavenged by  $\text{H}_2$  or NO which is important for obtaining highly dispersed catalysts from metal nitrate precursor salts.

CM702610H

(55) Yuvaraj, S.; Fan-Yuan, L.; Tsong-Huei, C.; Chuin-Tih, J. *Phys. Chem. B* **2003**, *107*, 1044–1047.

(56) Sietsma, J. R. A.; Meeldijk, J. D.; Den Breejen, J. P.; Versluijs-Helder, M.; Van Dillen, A. J.; De Jongh, P. E.; De Jong, K. P. *Angew. Chem., Int. Ed.* **2007**, *46*, 4547–4549.